Principal Modes of Atmospheric Variability in Model Atmospheres with and without Anomalous Sea Surface Temperature Forcing in the Tropical Pacific

IN-SIK KANG*

Geophysical Fluid Dynamics Program, Princeton University, Princeton, NJ 08542

NGAR-CHEUNG LAU

Geophysical Fluid Dynamics Laboratory/NOAA, Princeton University, Princeton, NJ 08542

(Manuscript received 2 January 1986, in final form 1 June 1986)

ABSTRACT

Principal modes of low-frequency atmospheric variability and the influence of sea surface temperature anomalies on such modes are investigated by examining the output from two general circulation model experiments. In the first experiment (the "control run"), all boundary forcings were constrained to evolve through 15 identical annual cycles. In the second experiment (the "SST runs"), the sea surface temperature conditions in the tropical Pacific Basin were prescribed to follow the actual month-to-month changes observed during the period 1962–76, which encompasses several El Niño events. The analysis tools employed here include empirical orthogonal functions, teleconnections and composite charts.

Two prominent modes of variability have been identified in the wintertime Northern Hemisphere eddy streamfunction of the SST experiment. The first mode bears a strong spatial resemblance to the observed characteristic circulation pattern over the North Pacific–North American sector. It is demonstrated that this mode is highly correlated with the changing SST forcing imposed over the tropical Pacific, and with various meteorological phenomena accompanying El Niño-Southern Oscillation (ENSO). The second mode exhibits no significant correlation with the SST forcing, but is linked instead to a characteristic structure of the zonally averaged zonal wind. The circulation features related to this mode are reminiscent of observed anomalies accompanying the North Atlantic Oscillation, as well as variations of the "zonal index." The fluctuations associated with the first and second modes in the SST experiment are of comparable amplitudes. It is further demonstrated that the essential characteristics of the first and second modes are highly reproducible in another 15-year simulation initiated from a completely independent set of atmospheric conditions.

A parallel diagnosis of the model behavior in the control run reveals no signal of the first mode (*i.e.*, that related to ENSO) as previously described. However, circulation features accompanying the second mode are still discernible in the control experiment. It is noted that the predominant anomalous phenomena in the control run are manifestations of the zonal/eddy relationship associated with the second mode. The mode appearing in both the control and SST runs is likely related to internal dynamical processes in the model atmosphere subjected to a fixed boundary forcing.

1. Introduction

The causes of low-frequency atmospheric variability may be classified into two broad categories: external forcing and dynamical processes within the atmosphere. Recent investigations using theoretical, modeling and observational tools have advanced our understanding of how fluctuations in the atmospheric circulation may be linked either to internal or external processes. For instance, the influences of anomalous sea surface temperature (SST) conditions on the tropospheric flow pattern have been demonstrated in many observational studies since the pioneering works of Bjerknes (1966, 1969) and Namias (1969), as well as in various numerical model experiments pursuant to the early results reported by Rowntree (1972) and Webster (1972). Other external factors which might lead to atmospheric fluctuations include changes in continental snow cover (Walsh et al., 1982), sea ice (Walsh and Johnson, 1979), and ground hydrology (Yeh et al., 1984). Notwithstanding the considerable evidence collected on the impact of various boundary forcing mechanisms, the correlation between the atmospheric signal and the external changes remains rather low in some instances. A case in point is the closely studied relationship between SST fluctuations in the equatorial Pacific and the characteristic wavelike flow pattern in the North Pacific–North American sector. The statistics presented by Horel and Wallace (1981) indicate that the tropical SST changes explain only about 25% of the temporal variance of an index

* Present affiliation: Department of Atmospheric Sciences, Seoul National University, Seoul, Korea.

depicting the strength and polarity of the previously mentioned wave pattern. It is hence likely that dynamical mechanisms operating within the atmosphere itself also play a substantial role in the atmospheric variability on monthly and seasonal time scales. Possible candidates in this category include wave-mean flow and wave–wave interactions, transitions among various equilibrium states, occurrence of unstable modes with slow growth rates, and formation of stable, long-lived flow configurations (see Wallace and Blackmon, 1983, for a comprehensive review).

The issue of boundary forcing versus internal atmospheric processes in causing circulation changes is brought into sharper focus by a series of extended general circulation model (GCM) experiments conducted at the Geophysical Fluid Dynamics Laboratory (GFDL). In the first 15-year experiment of this series (hereafter referred to as the *control run*), no interannual variability in the external forcing has been introduced. This control run has been analyzed by Manabe and Hahn (1981), who noted that, despite the absence of anomalous boundary forcing, the model atmosphere exhibits a level of variability comparable to that observed in middle and higher latitudes. A companion diagnostic study by Lau (1981) further indicates that the dominant spatial mode of variability appearing in this run is in reasonable agreement with its observed counterpart in the wintertime extratropical Northern Hemisphere. These results evidently call for an interpretation of the model variability in terms of internal processes.

More recently, another experiment using essentially the same GCM was performed with the SST conditions in the tropical Pacific being prescribed to follow the actual month-to-month changes observed during a 15-year period. Results of the latter integrations (hereafter referred to as the *SST runs*) have been reported by Lau and Oort (1985) and Lau (1985). It was demonstrated that the simulated variability in the tropics is noticeably enhanced in the presence of SST anomalies, and that the El Niño-Southern Oscillation (ENSO) episodes occurring within the 15-year period considered here are coincident with well-defined circulation anomalies in the model atmosphere. In particular, the wavelike response observed by Horel and Wallace (1981) in the North Pacific–North American sector during winter is well simulated. The findings from the SST runs thus argue for a substantial role for anomalous oceanic conditions in organizing the spatial modes of atmospheric variability.

It is evident from the foregoing discussion that both the control and SST runs yield recurrent circulation anomalies which bear a certain degree of resemblance to those observed in the real atmosphere. However, in view of the rather different boundary conditions under which these two types of integrations are conducted, the processes associated with the characteristic modes in the control experiment are probably different from the processes associated with modes in the SST runs. The primary objective of the present investigation is to highlight such differences by comparing in detail the spatial and temporal properties of the dominant modes of variability appearing in the control and SST runs, and by delineating the statistical relationships between these modes and selected meteorological parameters. The results presented herein should therefore shed more light on the nature of the anomalous model behavior reported earlier in Lau (1981, 1985).

For the sake of brevity, we shall focus our attention on the wintertime circulation in the Northern Hemisphere. In section 3, two prominent modes of variability in the 300-mb eddy streamfunction field for the first SST run are identified using empirical orthogonal functions. The connections of these two patterns with various ENSO-related meteorological phenomena, and with the dominant modal structure of the zonally averaged zonal flow, are explored in sections 4 and 5, respectively. The extent to which the relationships identified in sections 4 and 5 are reproducible in the second independent 15-year SST run is examined in section 6. In section 7, the foregoing results for the SST runs are then compared with the corresponding diagnosis performed on data from the control experiment, and inferences of such findings on the multiple causes of atmospheric variability are then drawn.

2. Description of the control and SST experiments

The GCM used for conducting both the control and SST experiments was developed and maintained by the Climate Dynamics Project at GFDL. Horizontal variations in the global model domain are represented spectrally in terms of spherical harmonics, with a rhomboidal truncation at 15 wavenumbers. Vertical variations are represented using nine sigma levels. Realistic land–sea contrast and orography have been incorporated in the lower boundary of the model. A comprehensive family of physical processes, including dry and moist convection, long- and shortwave radiation, ice-albedo feedback and ground hydrology, have been included. The prescribed cloud cover used in radiative transfer calculations is assumed to depend on height and latitude only. A detailed description of the model formulation has been given by Gordon and Stern (1982). Various aspects of the model climatology have been documented by Manabe and Hahn (1981) and Lau (1985).

In the control experiment (Manabe and Hahn, 1981), the external conditions for solar heating and sea surface temperature were set to their climatological seasonal values and prescribed to evolve through 15 identical annual cycles, so that these boundary forcings in a given calendar month of a certain year are exactly the same as the forcings in the same calendar month of any other year.

The SST experiment (Lau, 1985) is different from the control run in one important aspect: instead of

using climatological SST conditions throughout the world oceans, the lower model boundary over the tropical Pacific Basin between 30°S and 30°N was forced by monthly SST variations observed during the 15-year duration from 1962 to 1976, which encompasses four ENSO episodes with varying degrees of intensity. Altogether two such SST runs were completed. The only distinction between this pair of 15-year integrations is that they were initiated from completely independent atmospheric conditions. The relationships described in sections 3 to 5 are based on data from the first SST run only, so that data from the second SST run may be held in reserve for assessing the robustness of such relationships (see section 6).

3. Principal modes of variability in the first SST run

Since we are primarily concerned with fluctuations of the wavy flow field in the wintertime Northern Hemisphere, we shall first identify the characteristic anomalous patterns of the departure from zonal mean of the monthly averaged 300-mb streamfunction ψ^*. Monthly mean data from the first SST run for December, January and February will be examined here. For studying stationary waves in the global domain, the variable ψ^* chosen here is a more suitable quantity than geopotential height used in most observational studies, since the latter quantity tends to de-emphasize circulation features in the tropics and overemphasize perturbations in the extratropics. In this paper we shall use the term "eddy" to refer to departure from zonal symmetry. The analysis procedure is described as follows:

- A grid mesh similar to that used in Lau (1981, Fig. 5a) but covering the entire Northern Hemisphere and consisting of 160 points was designed, with each grid point representing an area more or less equal in size to that represented by any other grid point.
- The 15-year mean seasonal cycle was removed from the eddy streamfunction field.
- The anomaly values at a given grid point were normalized by the corresponding temporal standard deviation computed at the same grid point.
- The data set consisting of anomaly patterns for 45 winter months in the first SST run was subjected to an empirical orthogonal function (EOF) analysis. (See Kutzbach, 1967, for a concise description of the analysis procedures involved and the pertinent interpretations.)

In Fig. 1 are shown the patterns of the (a) first and (b) second spatial eigenvectors. These patterns, hereafter referred to as $e_1(\psi^*)$ and $e_2(\psi^*)$, explain 11.3% and 9.6% of the hemispherically integrated variance, respectively. Since the interpretation of such EOF patterns is often complicated by the somewhat artificial orthogonality constraints among different eigenvectors, we have also examined the structure of various one-point teleconnection maps, which depict the spatial distributions of temporal correlation coefficients between fluctuations at a given reference point and the corresponding fluctuations at all remaining grid points within the data domain. As was demonstrated by Wallace and Gutzler (1981), these teleconnection maps are particularly suited for identifying characteristic modal structures of a more local nature. Furthermore, such cross-correlation patterns are free of any orthogonality constraints. In Fig. 1c, d are shown the patterns of two such teleconnection maps based on 300-mb eddy streamfunction, with the reference points being located at 20.25°N, 172.5°W (point A in Fig. 1c) and 65.25°N, 150°W (point B in Fig. 1d), respectively. These particular sites correspond to the strongest extrema appearing in the patterns for $e_1(\psi^*)$ and $e_2(\psi^*)$, respectively. Comparisons between Fig. 1a and 1c, and between Fig. 1b and 1d, indicate that the two independent analysis tools (i.e., EOF and teleconnection maps) produce essentially the same spatial patterns. The strong resemblance noted here between each eigenvector and its associated teleconnection map establishes the EOF patterns shown in Fig. 1a, b as meaningful modal structures.

The pattern of $e_1(\psi^*)$ (Fig. 1a) is best characterized as a wave train spanning the Western Hemisphere. In particular, the circulation within the sector between 60°–180°W bears a strong resemblance to the Pacific/North American (PNA) pattern documented in the observational study of Wallace and Gutzler (1981). Locations of the centers of action used in the latter study for describing the observed PNA pattern (i.e., 20°N, 160°W; 45°N, 165°W; 55°N, 115°W; and 30°N, 85°W) are indicated in Fig. 1a, c by solid dots. It is evident from these figures that a close correspondence exists between the observed and model-generated centers. Henceforth we shall restrict the usage of the label "PNA pattern" to refer exclusively to the circulation pattern as defined in Wallace and Gutzler (1981), with the centers of action being located at the four grid points indicated in Fig. 1a, c.

A wavelike feature is also discernible in $e_2(\psi^*)$ (Fig. 1b, d) over the North Pacific and North America. However, a detailed comparison between $e_1(\psi^*)$ and $e_2(\psi^*)$ reveals subtle differences with respect to the precise geographical location of the nodes and antinodes. Whereas $e_1(\psi^*)$ exhibits extrema over the Aleutian Islands, western Canada and the United States Gulf Coast, the centers associated with $e_2(\psi^*)$ lie over the Alaskan Peninsula, the Hudson and Baffin bays, and off the eastern United States seaboard. Differences between $e_1(\psi^*)$ and $e_2(\psi^*)$ also exist over the Eurasian and Atlantic sectors.

In summary, two distinct circulation patterns which are orthogonal to each other in time and in space have been identified in the first SST run. The first mode $[e_1(\psi^*)]$ is similar to the observed PNA pattern in many respects, and is almost featureless in much of the East-

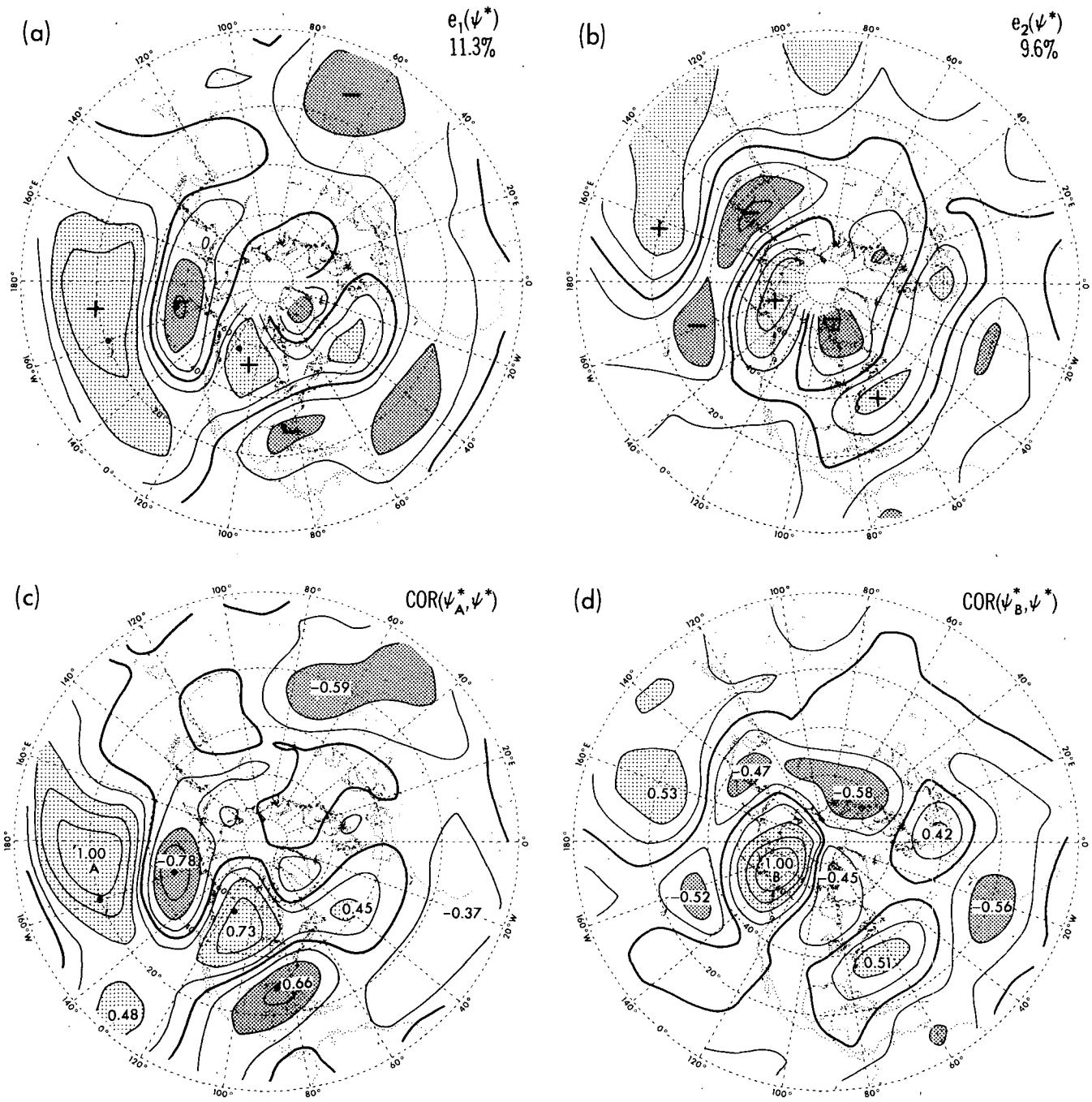

FIG. 1. Distributions of the (a) first [$e_1(\psi^*)$] and (b) second [$e_2(\psi^*)$] eigenvector of the 300-mb eddy streamfunction field (arbitrary units), and of the temporal correlation coefficients between fluctuations of the 300-mb eddy streamfunction at (c) 20.25°N, 172.5°W (point A) and (d) 65.25°N, 150°W (point B) and the corresponding fluctuations at all remaining grid points in the Northern Hemisphere, contour interval 0.2. All results are based on monthly means for 15 northern winters in the first SST run. Values greater than two times contour interval are indicated by light shading. Values less than minus two times contour interval are indicated by dark shading. The solid dots in panels a and c indicate the centers of action used by Wallace and Gutzler (1981) for constructing the PNA index.

ern Hemisphere. The second mode [$e_2(\psi^*)$] appears to have a relatively wider geographical extent, with centers of action located both over the Pacific/North American as well as the Eurasian sectors. Sections 4 and 5 are devoted to a more detailed diagnosis of the nature of these two characteristic patterns.

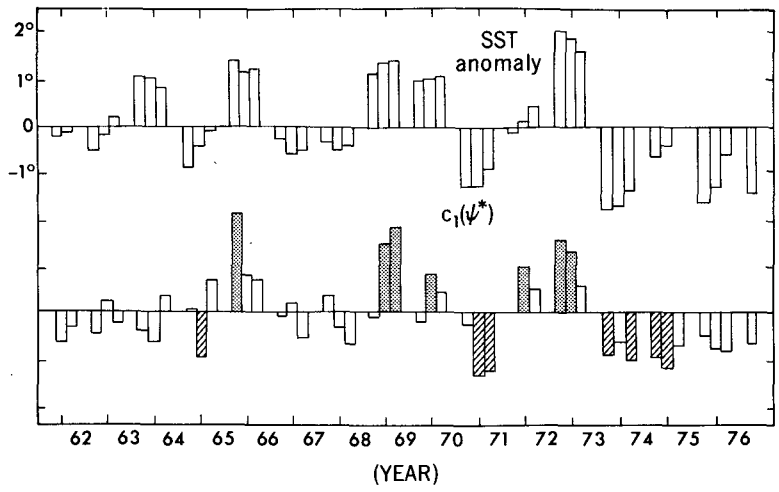

FIG. 2. Temporal variations during the 15 winters (1962–76) in the first SST run of monthly sea surface temperature anomalies averaged over the area extending from 4.5°S to 4.5°N, and from 180°E to 135°W, (upper-half, units: °C); and monthly coefficients for $e_1(\psi^*)$ (lower-half, arbitrary units). Those 7 months with the most positive (negative) eigenvector coefficients are identified by stippled (striped) columns in the lower-half, and used to construct the composite chart in Fig. 3. Tick marks along the x-axis indicate the January of each year.

4. Association of the $e_1(\psi^*)$ pattern with ENSO phenomena

Horel and Wallace (1981), van Loon and Rogers (1981) and Chen (1982), among others, have provided much observational evidence linking the ENSO phenomena with the wintertime PNA pattern. As has been demonstrated in Lau (1985, Figs. 12 and 13), this relationship is well simulated in the SST experiment. The considerable resemblance noted in the previous section between $e_1(\psi^*)$ in the first SST run and the observed PNA pattern indicates that this mode may be viewed as the Northern Hemisphere response during the mature phase of ENSO events.

In Fig. 2 are shown the month-to-month variations during the 15 winters (1962–76) of both the prescribed SST anomaly averaged over the equatorial Pacific strip extending from 4.5°S to 4.5°N and from 180°E to 135°W, and also the coefficients associated with $e_1(\psi^*)$ [hereafter referred to as $c_1(\psi^*)$]. These two indices evidently exhibit a strong temporal correlation, with warm SST anomalies during the 1965/66, 1969/70 and 1972/73 El Niños being accompanied by positive $c_1(\psi^*)$ (i.e., anticyclonic flows over the subtropical Pacific and western Canada, and cyclonic flows over the Aleutians and southeastern United States, see Fig. 1a), and vice versa. The correlation coefficient between the monthly means in the pair of time series shown here is 0.74, and exceeds the 99% significance level.[1] The correlation cited here may be compared with the corresponding observed value of 0.46 between the seasonally averaged PNA and Pacific SST indices for the 1951–78 period, as reported by Horel and Wallace (1981, Table 1).

The SST index chosen for presentation in Fig. 2 mainly describes the anomalous oceanic forcing in the central equatorial Pacific (180°E to 135°W, hereafter referred to as SSTC). Modeling studies by Palmer and Mansfield (1984) indicate that the midlatitude circulation also exhibits considerable sensitivity to SST anomalies located in the equatorial Pacific *west* of the dateline. The dependence of the extratropical response to the geographical location of the tropical Pacific SST forcing was also demonstrated in the GCM experiments examined by Geisler et al. (1985). In order to discern the relationships of various atmospheric modes to the oceanic conditions in different sectors of the equatorial Pacific, two additional SST indices have been considered. These indices are constructed using the areal averages of the SST anomaly in the western equatorial

TABLE 1. Matrix of temporal correlation coefficients between the EOF coefficients $c_1(\psi^*)$, $c_2(\psi^*)$, $c_1(\bar{u})$, and the indices describing the SST anomalies in the western (SSTW), central (SSTC) and eastern (SSTE) equatorial Pacific. (See text.) All computations were based on monthly mean data for the 15 northern winters in the first SST run.

	$c_1(\psi^*)$	$c_2(\psi^*)$	$c_1(\bar{u})$
SSTW	0.44	−0.14	−0.27
SSTC	0.74	0.15	0.02
SSTE	0.67	0.11	0.01
$c_1(\bar{u})$	−0.12	0.57	1.00

[1] Assuming that there are two degrees of freedom in each 3-month winter season, the threshold values for the correlation coefficient at the 95% and 99% significance levels are 0.31 and 0.42, respectively.

Pacific (4.5°S to 4.5°N, 135°E to 180°E; hereafter referred to as SSTW) and the eastern equatorial Pacific (4.5°S to 4.5°N, 135°W to 90°W; hereafter referred to as SSTE). The temporal correlations between $c_1(\psi^*)$ and all three SST indices are displayed in the first column of Table 1. It is seen that $c_1(\psi^*)$ is positively correlated with the SST variations throughout the equatorial Pacific. The degree of correlation is strongest in the central Pacific (SSTC), and noticeably weaker in regions farther west (SSTW).

The typical amplitudes at individual centers of action associated with $e_1(\psi^*)$ are illustrated by the composite chart in Fig. 3. This pattern is constructed by subtracting the average of the anomalous eddy streamfunction for the 7 winter months with the most negative $c_1(\psi^*)$ (indicated in Fig. 2 by striped columns) from the corresponding quantity for the 7 months with the most positive $c_1(\psi^*)$ (indicated by stippled columns). Inspection of Fig. 2 indicates that most of the months thus chosen fall within periods of large SST anomalies. The scaled maxima and minima shown in Fig. 3 need to be multiplied by 10 to yield the corresponding amplitudes of extratropical geopotential height perturbations in units of meters. The centers of action associated with the observed PNA pattern are again indicated by solid dots in Fig. 3. The peak-to-peak amplitudes at these four centers are equivalent to approximately 100 m of geopotential height. These es-

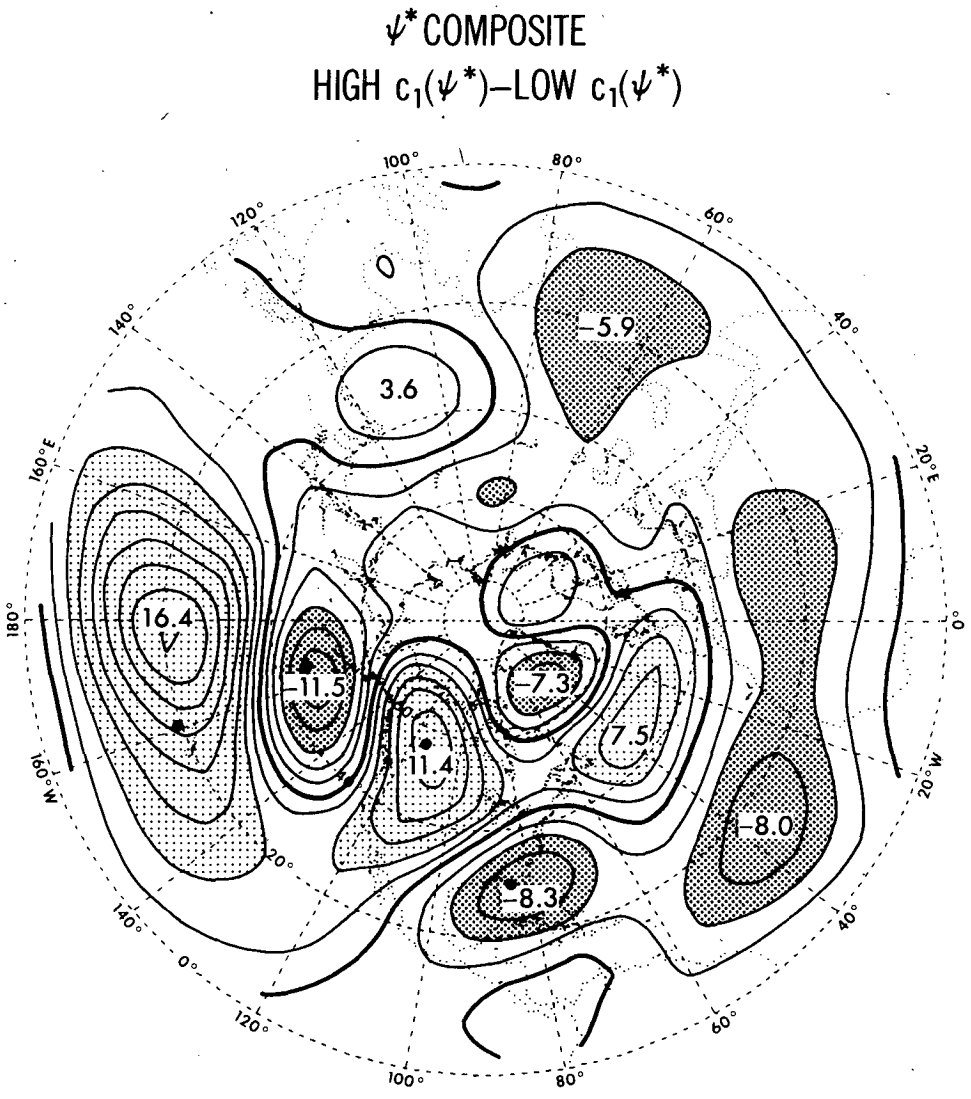

FIG. 3. Composite chart for 300-mb eddy streamfunction in the first SST run, as obtained by subtracting averages for the 7 months with the most negative coefficients of $e_1(\psi^*)$ (striped columns in lower half of Fig. 2) from the corresponding values for the 7 months with the most positive coefficients (stippled columns in Fig. 2). Contour interval 2×10^6 m^2 s^{-1}. The solid dots indicate the centers of action used by Wallace and Gutzler (1981) for constructing the PNA index.

timates are consistent with the half-amplitude values reported in Lau (1985, Fig. 13a) based on averages over all simulated ENSO winters, and with the observed data presented by van Loon and Rogers (1981, Fig. 4) and Chen (1982, Figs. 7 and 8). As expected, the composite pattern in Fig. 3 is almost identical to that of $e_1(\psi^*)$ (Fig. 1a). The horizontal tilt of the trough and ridge axes associated with the wave pattern is suggestive of poleward energy propagation over the Pacific, and equatorward propagation over North America. It is also apparent from Fig. 3 that warm SST winters tend to coincide with easterly anomalies in the upper troposphere over the equatorial Pacific, and with strengthening of the Pacific jet stream within the 30°–50°N latitude zone. As noted earlier, the fluctuations over most of the Eastern Hemisphere are characterized by much weaker amplitudes.

As additional evidence on the relationship between $e_1(\psi^*)$ and ENSO, in Fig. 4 are presented the distributions of temporal correlation coefficients between monthly means of $c_1(\psi^*)$ (i.e., the time series shown in the lower half of Fig. 2) and the local values of (a) 1000-mb height, (b) 1000–200-mb thickness, (c) precipitation, and (d) 300-mb total streamfunction (with zonal means retained). All computations are based on 45 northern winter months in the first 15-year SST run. The monthly averaged precipitation data have been smoothed spatially by retaining only fluctuations with zonal wavenumbers of 6 or smaller.

The teleconnection charts in Fig. 4 reveal many of the well-known meteorological anomalies occurring in the mature warm phase of the ENSO cycle, both in the observed atmosphere [e.g., see Horel and Wallace (1981), Rasmusson and Carpenter (1982), and Arkin

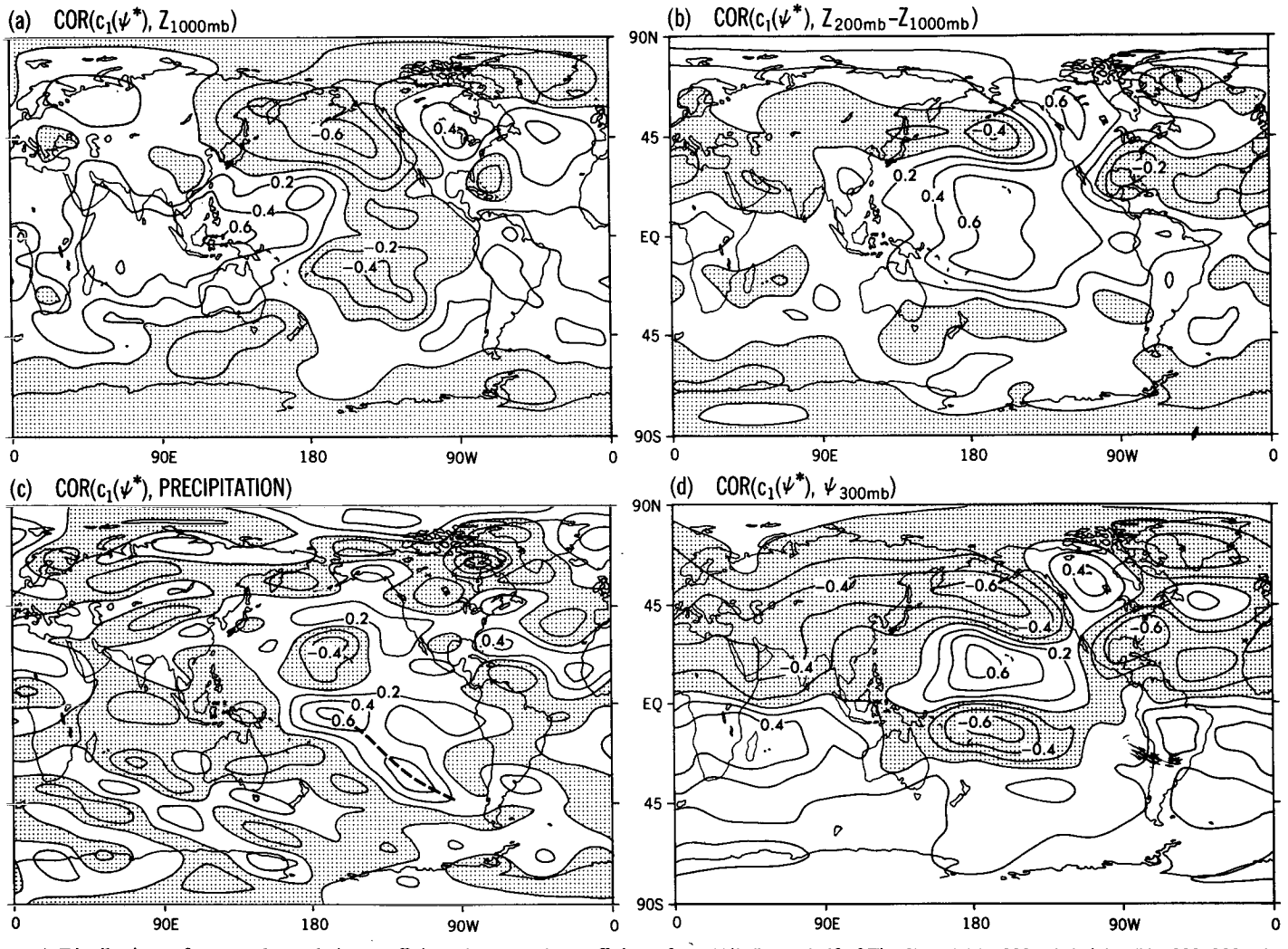

FIG. 4. Distributions of temporal correlation coefficients between the coefficients for $e_1(\psi^*)$ (lower half of Fig. 2) and (a) 1000-mb height, (b) 1000–200-mb thickness, (c) precipitation rate and (d) 300-mb total streamfunction. Contour interval is 0.2. All results are based on monthly means for 15 northern winters in first SST run. The dashed line in panel c indicates the position of the South Pacific Convergence Zone during the warm phase of the ENSO events. Negative values are shaded.

(1982)] and in the SST experiment (Lau, 1985). Within the tropical belt, positive $c_1(\psi^*)$ are seen to be accompanied by the following model features:

- a dipolar signal in the 1000-mb height field, with below-normal values over the Pacific east of the dateline, and above-normal values over the western Pacific, Indonesia, northern Australia and the Indian Ocean (Fig. 4a);
- above-normal 1000–200 mb thickness throughout the entire equatorial belt, with particularly enhanced correlations over the central Pacific (Fig. 4b);
- above-normal precipitation over the equatorial Pacific at and east of the dateline, and suppressed rainfall over Indonesia, the Indian Ocean, as well as the subtropical North Pacific just west of the Hawaiian Islands (Fig. 4c). Eastward migration of the South Pacific convergence zone, leading to enhanced precipitation along a belt in the South Pacific oriented in the southeast–northwest direction (indicated by a dashed line in Fig. 4c), and dryness in the region located farther west;
- formation of a pair of anticyclones at 300 mb straddling the equatorial Pacific, with anomalous easterlies over the equator, and anomalous westerlies in the subtropical Pacific of both hemispheres.

The polarities of all the anomalies described above would be reversed in periods corresponding to negative $c_1(\psi^*)$.

Within the Northern Hemisphere extratropics, the teleconnection patterns for geopotential height, thickness and streamfunction fields (Fig. 4a, b, d) are dominated by a wavelike feature spanning the Pacific Ocean and North America. Intercomparison between these charts indicates a mostly equivalent barotropic vertical structure for this pattern, with cyclonic flows in the upper troposphere coinciding with low thicknesses and low surface pressures, and vice versa.

The evidence presented in this section (Figs. 2–4) clearly indicates that the characteristic pattern which explains the largest fraction of the variance in the 300-mb eddy streamfunction field is indeed closely related to the time varying SST forcing imposed in the tropical Pacific.

5. Association of the $e_2(\psi^*)$ pattern with variability of the zonally averaged circulation

The spatial pattern for $e_2(\psi^*)$ (Fig. 1b, d) exhibits some noticeable differences from the characteristic model response during ENSO (cf. Lau, 1985, Fig. 13a). As is evident from the second column of Table 1, the correlations between the coefficients of $e_2(\psi^*)$, hereafter referred to as $c_2(\psi^*)$ (see lower half of Fig. 6), and the variations of SSTW, SSTC and SSTE are uniformly low. Hence the $e_2(\psi^*)$ mode is apparently not related to the anomalous oceanic conditions imposed in the entire equatorial belt between 135°E and 90°W. By considering the linearized, steady state conservation equation for absolute vorticity, Branstator (1984) noted that, for a fixed external forcing, a well-defined relationship exists between departures of the steady flow from zonal symmetry (i.e., the "eddy" component examined in our study) and the zonally averaged zonal wind. He has further demonstrated this "zonal/eddy" relationship using observational data and solutions of a linear barotropic model. In this section we shall determine whether the $e_2(\psi^*)$ pattern may be interpreted in terms of such a zonal/eddy relationship.

Figure 5 shows the meridional structure of the first eigenvector of the wintertime Northern Hemisphere zonally averaged zonal wind $\bar{u}$ at 300 mb in the first SST run. A procedure similar to that used for obtaining $e_1(\psi^*)$ and $e_2(\psi^*)$ was adopted here, with the exception that the EOF analysis has been applied to monthly mean data for $\bar{u}$ at 20 equally spaced latitudes extending from 2.25° to 87.75°N. The modal structure in Fig. 5, hereafter referred to as $e_1(\bar{u})$, explains 38.2% of the total variance. It depicts an out-of-phase relationship between fluctuations in the zonally averged subtropical jet stream at 30°–35°N and those in the zonal flow at 55°–65°N. This behavior is in agreement with the observed structure of the first eigenvector of the zonal mean flow presented by Branstator (1984, Fig. 2a) based on NMC analyses for 15 winters.

The coefficients displayed in Table 1 indicate that the temporal variation of the coefficients of $e_1(\bar{u})$, hereafter referred to as $c_1(\bar{u})$, exhibits negligible correlation with the oceanic conditions in the eastern and central equatorial Pacific (SSTE and SSTC), and with the time series $c_1(\psi^*)$. The correlation between $c_1(\bar{u})$ and SSTW (−0.27) is stronger, but is nonetheless still below the 95% significance level (see footnote 1).

The relationship between $e_1(\bar{u})$ and $e_2(\psi^*)$ in the first SST run is delineated in Fig. 6, which shows in juxtaposition temporal variations of the coefficients of these two eigenvectors, $c_1(\bar{u})$ and $c_2(\psi^*)$. A considerable degree of resemblance apparently exists between these two time series. The corresponding temporal correlation coefficient of 0.57 (see Table 1) is significant at the 99% confidence level. Hence this result suggests

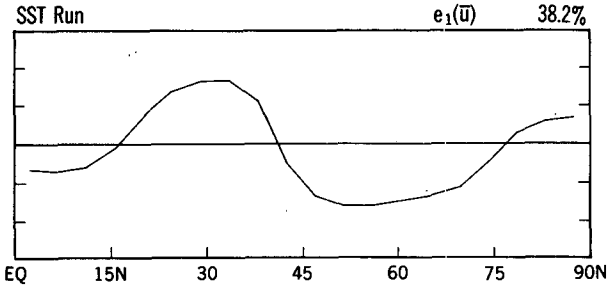

FIG. 5. Distribution of the first eigenvector of the zonally averaged zonal wind at 300 mb, $e_1(\bar{u})$, as computed using monthly means for 15 northern winters in the first SST run. Arbitrary units.

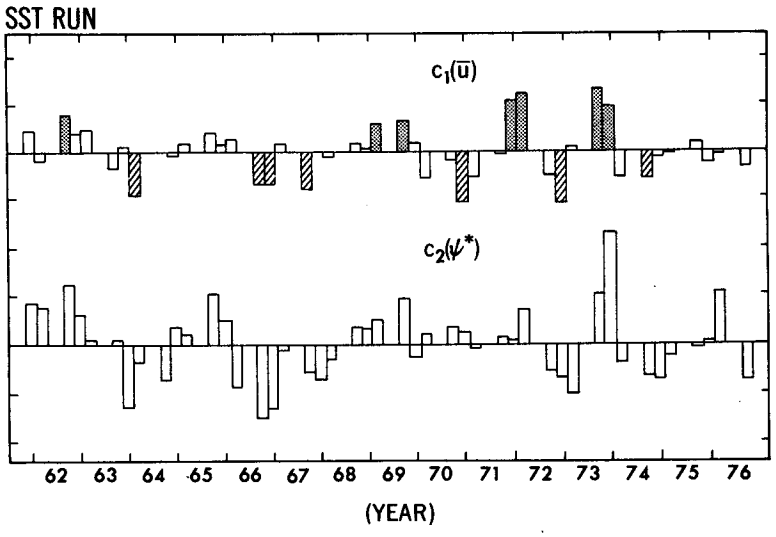

FIG. 6. Temporal variations during the 15 winters in the first SST run of the coefficients for $e_1(\bar{u})$ (upper-half); and of the coefficients for $e_2(\psi^*)$ (lower-half). Arbitrary units. Those seven months with the most positive (negative) coefficients for $e_1(\bar{u})$ are identified by stippled (striped) columns in the upper-half, and are used to construct the composite charts in Fig. 7.

that $e_2(\psi^*)$ is linked to the dominant mode of variability of the zonally averaged zonal flow.

As additional evidence for the zonal/eddy relationship between $e_1(\bar{u})$ and $e_2(\psi^*)$, in Fig. 7a is shown the composite chart for 300-mb eddy streamfunction ψ^*. This pattern depicts the difference between the averaged ψ^* field during the seven months with the largest positive $c_1(\bar{u})$ and the seven months with the largest negative $c_1(\bar{u})$. The months used in constructing this chart are indicated in the upper half of Fig. 6 by stippled and striped columns. The composite chart for 300-mb total zonal wind, as obtained using the same procedure as above and retaining both the zonal mean and eddy contributions to u, is shown in Fig. 7b. It is seen that Fig. 7a exhibits a strong spatial resemblance to $e_2(\psi^*)$ and the associated teleconnection chart (Fig. 1b, d). In the extratropics, the amplitudes of the centers of action in Fig. 7a are comparable to those in the composite pattern for $e_1(\psi^*)$ (Fig. 3). However, the tropical features associated with $e_2(\psi^*)$ are considerably weaker than their counterparts in $e_1(\psi^*)$. The composite chart for the total zonal wind (Fig. 7b) is noted for its considerable zonal symmetry. The nodal lines along the 20° and 40°N latitude circles are consistent with the meridional profile of $e_1(\bar{u})$ (Fig. 5). The most significant departure from zonal symmetry is found over the North Pacific. The dipole-like zonal wind anomaly over that region is consistent with the configuration of the eddy streamfunction pattern in Fig. 7a. This feature portrays the occasional advance and retreat of the climatological East Asian jet stream in the zonal direction, as well as the meridional shifts in the position of the jet stream axis.

The composite pattern for ψ^* based on model data (Fig. 7a) may be compared with the corresponding distribution obtained by applying a similar procedure to observations (Branstator, 1984, Fig. 4). Whereas some correspondence between simulated and observed features is noticeable over the midlatitude Pacific and Eurasia, there are also considerable discrepancies over North America and the Atlantic, where the centers of action in the model pattern are displaced too far north of their observed positions.

The circulation features associated with $e_1(\bar{u})$ [and hence $e_2(\psi^*)$] are further illustrated in Fig. 8, which shows the distributions of temporal correlation coefficients between $c_1(\bar{u})$ (upper half of Fig. 6) and monthly mean perturbations of (a) 1000-mb height, (b) 1000–200-mb thickness, (c) precipitation, and (d) total streamfunction (with both the zonal mean and eddy components included). Again the precipitation data have been smoothed spatially by retaining only fluctuations with zonal wavenumbers of 6 or smaller. Since these correlation values are generally weak in the Southern Hemisphere, only the Northern Hemisphere patterns are displayed here. The features appearing in Fig. 8 may be compared with those in the corresponding charts associated with $e_1(\psi^*)$ (Fig. 4).

The correlation pattern for 1000-mb height (Fig. 8a) is characterized by a north–south seesaw with a strong degree of zonal symmetry. The height changes along the 30°–40°N latitude belt are opposite to those in the polar cap north of 50°N. This anomaly pattern bears some resemblance to the dominant mode of variability in the observed hemispheric sea-level pressure field, as described by Kutzbach (1970, Fig. 1a), van Loon and

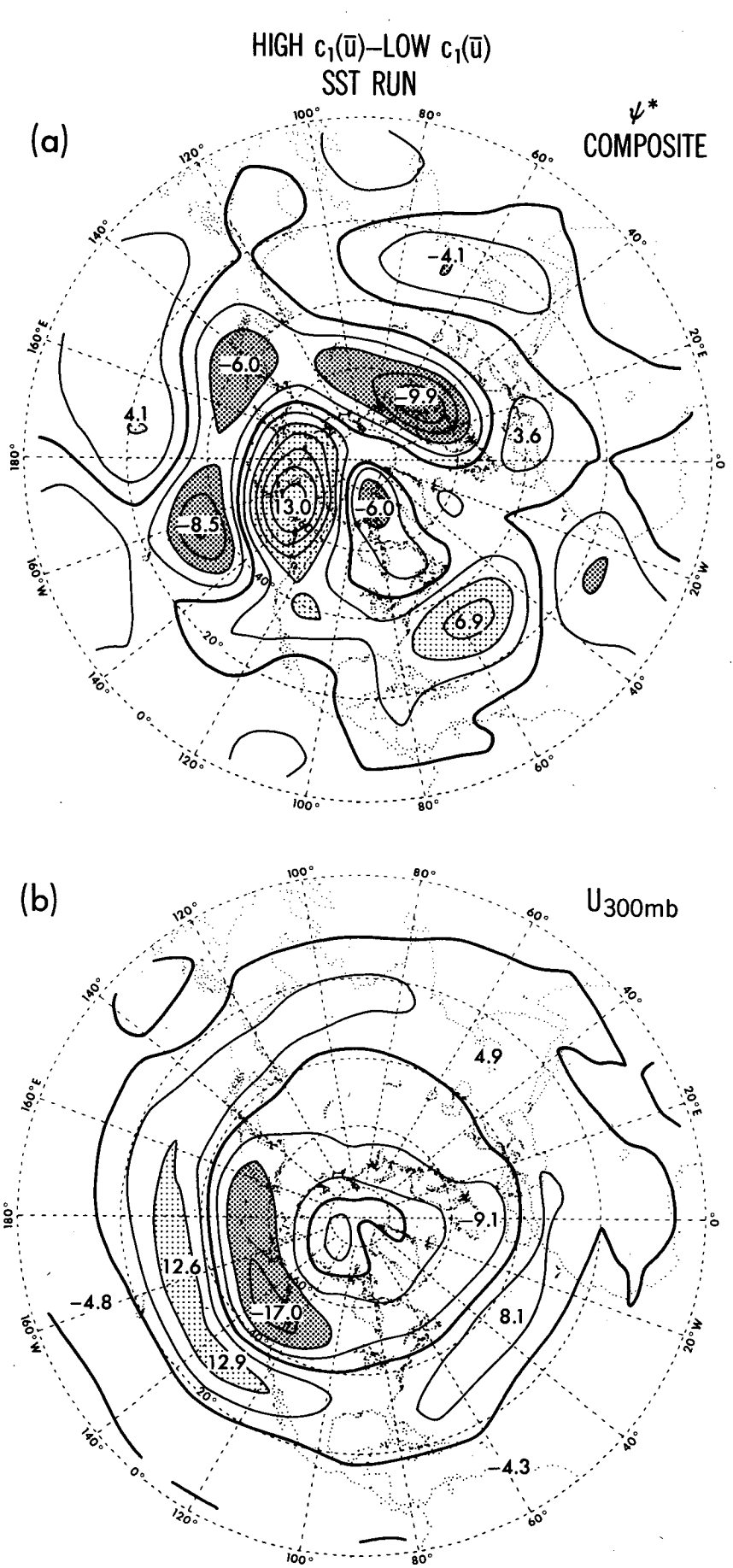
HIGH $c_1(\bar{u})$–LOW $c_1(\bar{u})$
SST RUN
(a)
ψ^*
COMPOSITE
-4.1
-6.0
-9.9
4.1
3.6
13.0
-6.0
-8.5
6.9
(b)
U_{300mb}
4.9
-9.1
12.6
-4.8
-17.0
8.1
12.9
-4.3

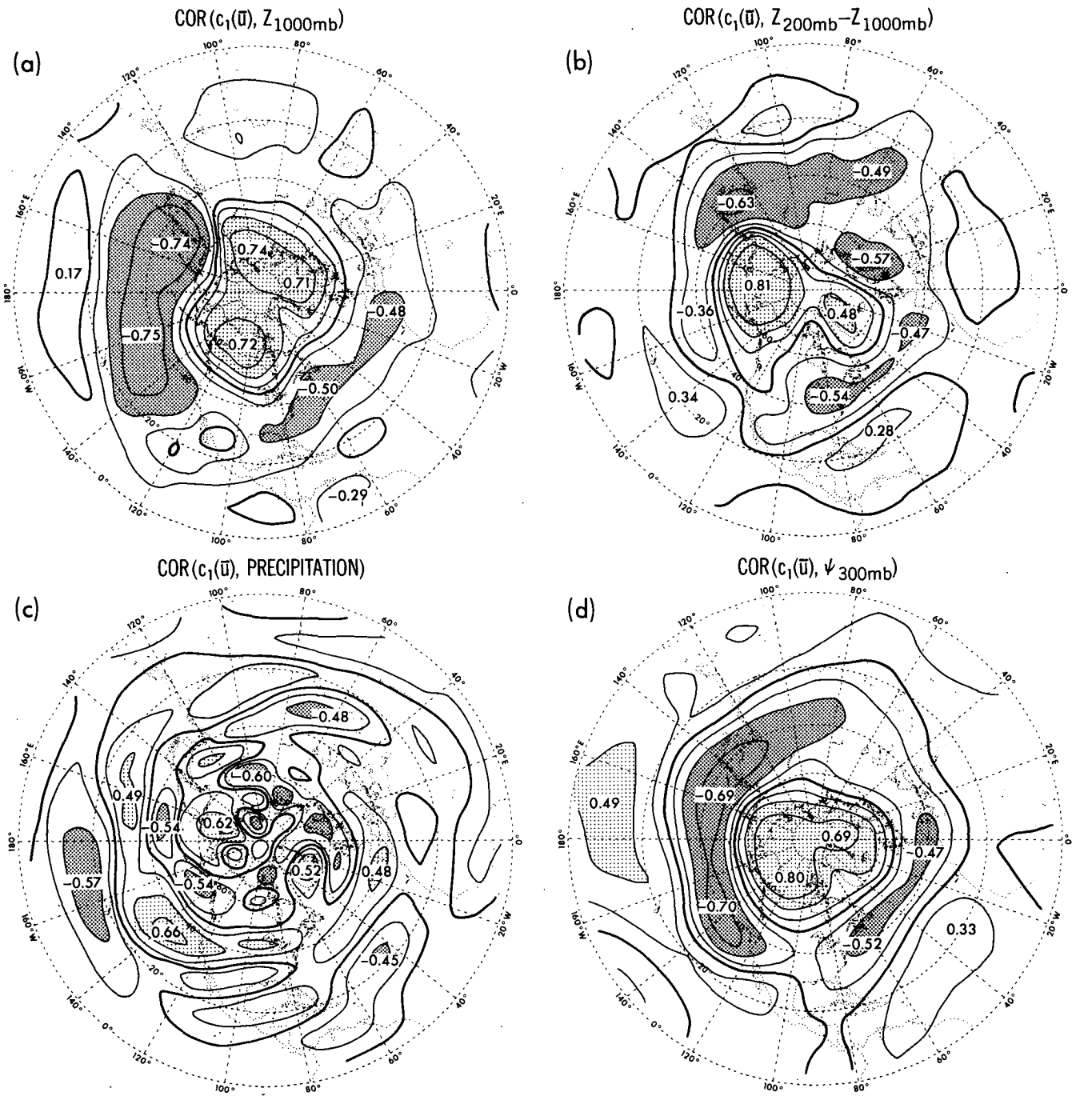

FIG. 8. As in Fig. 4, except for correlations with the coefficients for $e_1(\bar{u})$ (upper-half of Fig. 6) and for results in the Northern Hemisphere only. Values greater than 0.4 and less than −0.4 are indicated by light and dark shading, respectively.

FIG. 7. Composite chart for 300-mb (a) eddy streamfunction, contour interval 2×10^6 m^2 s^{-1}, and (b) total zonal wind, contour interval 5 m s^{-1}, as obtained by subtracting averages for the 7 months with the most negative coefficients of $e_1(\bar{u})$ (striped columns in upper-half of Fig. 6) from the corresponding values for the 7 months with the most positive coefficients (stippled columns in Fig. 6).

Rogers (1978) and Wallace and Gutzler (1981, Fig. 4), among others.

In contrast to the prominent changes in the thickness field over the tropics during ENSO (see Fig. 4b), $c_1(\bar{u})$ exhibits negligible correlations with the same field in the region south of 20°N (Fig. 8b). The pattern in Fig. 8b indicates that $e_1(\bar{u})$ is associated with well-defined seesaws in 1000–200 mb thickness between Greenland and northern Europe, as well as between the Great Lakes region of North America and the Bering Sea. These features are similar to the temperature changes accompanying the North Atlantic Oscillation in the observed atmosphere, as documented by Walker and Bliss (1932) and van Loon and Rogers (1978, Fig. 9).

The most notable features in the correlation pattern for precipitation (Fig. 8c) are the zonally oriented belts over the midlatitude oceans. Comparison between this chart and the 1000-mb height changes associated with $c_1(\bar{u})$ (Fig. 8a) indicates that enhanced rainfall tends to accompany negative surface pressure anomalies, and vice versa. The rainfall pattern in the North Atlantic–European sector agrees well with the shifts in precipitation zones associated with the observed east–west temperature seesaw in that region (see Rogers and van Loon, 1979, Fig. 5).

The correlation patterns for 1000-mb height, 1000–200-mb thickness and 300-mb streamfunction (Fig. 8a, b, d) are reminiscent of several meteorological phenomena associated with variations of the "zonal index," as discussed by Rossby and Willet (1948) and Namias (1950). It is seen that low index situations tend to prevail in periods with positive $c_1(\bar{u})$, with below normal meridional surface pressure gradients between 35° and 55°N (Fig. 8a), below normal temperatures in middle latitudes and strong baroclinicity in the subtropics (Fig. 8b), as well as an expanded polar vortex and strong westerlies near 30°N (Fig. 8d).

6. Reproducibility of results in the second SST run

In order to test the reproducibility of the statistical relationships discerned from the first SST run, a set of correlation coefficients analogous to those shown in Table 1 have been evaluated based on data for the second SST run. For an unambiguous comparison with the results presented thus far, we have chosen to examine various time series of spatial "dot products" between the predetermined eigenvectors shown in the previous sections and the corresponding monthly mean fields from the second SST run. Specifically, for each Northern Hemisphere winter month in the second SST run, the following quantities have been computed:

$$\langle e_1(\psi^*) \cdot \psi^*_{II} \rangle \equiv \sum_{i=1}^{160} [e_1(\psi^*)]_i [\psi^*_{II}]_i$$

$$\langle e_2(\psi^*) \cdot \psi^*_{II} \rangle \equiv \sum_{i=1}^{160} [e_2(\psi^*)]_i [\psi^*_{II}]_i$$

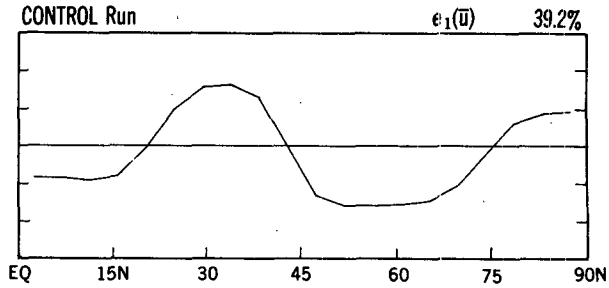

FIG. 9. As in Fig. 5, except for data from the control run.

$$\langle e_1(\bar{u}) \cdot \bar{u}_{II} \rangle \equiv \sum_{i=1}^{20} [e_1(\bar{u})]_i [\bar{u}_{II}]_i$$

Here $[X]_i$ denotes the value of $[X]$ at the ith grid point or latitude, the subscript II in ψ^*_{II} and $\bar{u}_{II}$ indicates that these eddy streamfunction and zonal mean wind fields pertain to the *second* SST run, whereas $e_1(\psi^*)$, $e_2(\psi^*)$ and $e_1(\bar{u})$ are the leading eigenvectors determined for the *first* SST run (i.e., those patterns depicted in Figs. 1a, 1b and 5, respectively). For the eddy streamfunction data, the summation is performed over the 160 points in the Northern Hemisphere grid mesh used for constructing $e_1(\psi^*)$ and $e_2(\psi^*)$ (see section 3). For the zonal mean wind data, the summation is performed over the 20 northern latitudes used for constructing $e_1(\bar{u})$ (see section 5). For a given northern winter month in the second SST run, the dot products as defined above provide appropriate measures of the spatial resemblance between the circulation pattern in that month and the dominant modes of variability documented in sections 3 and 5. These dot products are therefore analogous to the EOF coefficients analyzed in Table 1.

The time series of the dot products thus computed were then correlated with each other, as well as with the three tropical Pacific SST indices defined in section 4. The results are summarized in Table 2. Comparison between Tables 1 and 2 confirms that the relationships identified in the previous sections are equally evident in the second SST run. In particular, eddy streamfunction patterns resembling $e_1(\psi^*)$ are seen to be highly correlated with SSTC and SSTE, whereas perturbations similar to $e_2(\psi^*)$ are associated with variability of the zonal mean circulation [i.e., $e_1(\bar{u})$]. It is also worth noting that the somewhat marginal correlation (−0.27) between $e_1(\bar{u})$ and SSTW in Table 1 is even weaker in the second SST run (0.08), further substantiating our earlier claim that $e_1(\bar{u})$ and $e_2(\psi^*)$ are not systematically related to anomalous SST conditions imposed anywhere along the equatorial Pacific.

7. Principal mode of variability in the control run

Since $e_2(\psi^*)$ and $e_1(\bar{u})$ are only weakly correlated with the SST forcing prescribed in various sectors of the equatorial Pacific (see Tables 1 and 2), the SST

TABLE 2. Matrix of temporal correlation coefficients between the spatial dot products $\langle e_1(\psi^*)\cdot\psi^*_{II}\rangle$, $\langle e_2(\psi^*)\cdot\psi^*_{II}\rangle$, $\langle e_1(\bar{u})\cdot\bar{u}_{II}\rangle$, and the indices describing the SST anomalies in the western (SSTW), central (SSTC) and eastern (SSTE) equatorial Pacific. The eigenvectors $e_1(\psi^*)$, $e_2(\psi^*)$ and $e_1(\bar{u})$ were determined from the first SST run, and ψ^*_{II}, $\bar{u}_{II}$ represent monthly mean data of eddy streamfunction and zonal mean winds from the second SST run. [See text (section 6) for further details.]

	$\langle e_1(\psi^*)\cdot\psi^*_{II}\rangle$	$\langle e_2(\psi^*)\cdot\psi^*_{II}\rangle$	$\langle e_1(\bar{u})\cdot\bar{u}_{II}\rangle$
SSTW	0.39	−0.08	0.08
SSTC	0.72	0.09	0.18
SSTE	0.69	0.09	0.20
$\langle e_1(\bar{u})\cdot\bar{u}_{II}\rangle$	0.04	0.48	1.00

anomalies do not appear to play a substantial role in these particular modes. It is hence likely that the zonal/eddy relationship described in section 5 is also present in the control run, which has been conducted in the absence of any interannual variability in the oceanic conditions. This hypothesis is tested in the present section by applying a similar set of analysis tools to Northern Hemisphere wintertime data from the 15-year control experiment. The diagnosis performed here will not only improve our understanding of the zonal/eddy relationship revealed in this study, but also shed more light on the recurrent meteorological features in the control run noted by Lau (1981).

In Fig. 9 is a display of the meridional structure of the first eigenvector of the zonally averaged zonal wind, as computed using data from the control run for 45 winter months. This leading eigenvector, hereafter referred to as $e_1(\bar{u})^{\text{CONTROL}}$, accounts for 39.2% of the total variance. The profile shown here is almost identical to that based on data from the SST run (Fig. 5). Hence the characteristic modal structure of the zonal mean flow examined in section 5 is clearly discernible in the control run.

The hemispheric flow pattern associated with $e_1(\bar{u})^{\text{CONTROL}}$ is illustrated in Fig. 10, which shows the distribution of the temporal correlation coefficient between the coefficients for $e_1(\bar{u})^{\text{CONTROL}}$, hereafter referred to as $c_1(\bar{u})^{\text{CONTROL}}$, and the 300-mb total streamfunction (with both the zonal mean and eddy components included). This pattern bears a strong spatial resemblance to the corresponding correlation chart based on data for the SST run (Fig. 8d), hence suggesting the presence of an analogous zonal/eddy relationship in the control run. It is also seen that Fig. 10 is very similar to the circulation pattern associated with the principal anomaly complex discussed in Lau (1981, Fig. 14) based on data from the control run. The new evidence presented here thus reveals that the anomalous model behavior described in that earlier study is actually related to fluctuations in the zonally averaged zonal wind, and that the presence of anomalous external forcing is not an essential prerequisite for such a zonal/eddy relationship.

In order to determine how effective is the pattern shown in Fig. 10 in depicting the atmospheric variability in the control run, an EOF analysis has been performed on 300-mb eddy streamfunction data from that experiment using the procedure outlined in section 3. In Fig. 11 is shown the first eigenvector of the wintertime eddy streamfunction, $e_1(\psi^*)^{\text{CONTROL}}$, which explains 13.4% of the total variance. Taking into consideration that the zonal mean component has been removed from this analysis, one discerns that a close correspondence exists between some of the centers of action in Fig. 11 and those in Fig. 10. The pattern of Fig. 11 also compares well with the eddy component of the first eigenvector of 500-mb height, as shown in Lau (1981, Fig. 5). Hence changes in the zonal mean flow depicted by $e_1(\bar{u})^{\text{CONTROL}}$ (Fig. 9) are indeed associated with the dominant mode of the eddy streamfunction field in the control run. This relationship is further illustrated by the time series of the coefficients for $e_1(\bar{u})^{\text{CONTROL}}$ and $e_1(\psi^*)^{\text{CONTROL}}$ [i.e., $c_1(\bar{u})^{\text{CONTROL}}$ and $c_1(\psi^*)^{\text{CONTROL}}$], shown in Fig. 12. The high temporal correlation coefficient between these time series (0.72) easily surpasses the threshold corresponding to the 99% significance level (see footnote 1). A similarly high level of correlation is also apparent between the time series presented here and those associated with the principal anomaly mode diagnosed in Lau (1981, Fig. 12).

The composite charts for eddy streamfunction and total zonal wind, as constructed by mapping the differences between the seven months in the control run with the most positive $c_1(\bar{u})^{\text{CONTROL}}$ and the seven months with the most negative $c_1(\bar{u})^{\text{CONTROL}}$ (see stippled and striped columns in the upper half of Fig. 12), are presented in Fig. 13. These patterns may be compared with their counterparts for the SST run (Fig. 7). Whereas the amplitudes of the eddy streamfunction anomalies depicted in Figs. 7a and 13a are comparable, and individual anomaly centers in one chart may be matched with those in the other chart, there exists some discrepancies in the exact locations of various centers of action, particularly over the Atlantic. The differences noted here could be the result of inadequate data sampling within 15-winter data sets, although the likelihood of the modification of the zonal/eddy relationship in the presence of anomalous SST forcing cannot be ruled out. The correspondence between the zonal wind composites in the two runs (Figs. 7b and 13b) is better, with both patterns being characterized by zonally elongated bands over the Pacific and Atlantic. The most notable difference is that the amplitudes of the wind anomalies in the control run over the Atlantic are higher than those in the SST run by a factor of 2. The strong eddy streamfunction perturbations over the Atlantic and central Asia (Fig. 13a) are likely to be associated with the strong zonal wind changes over the Atlantic.

Correlation charts depicting changes of 1000-mb height, 200–1000-mb thickness and precipitation associated with $e_1(\bar{u})^{\text{CONTROL}}$ have also been constructed.

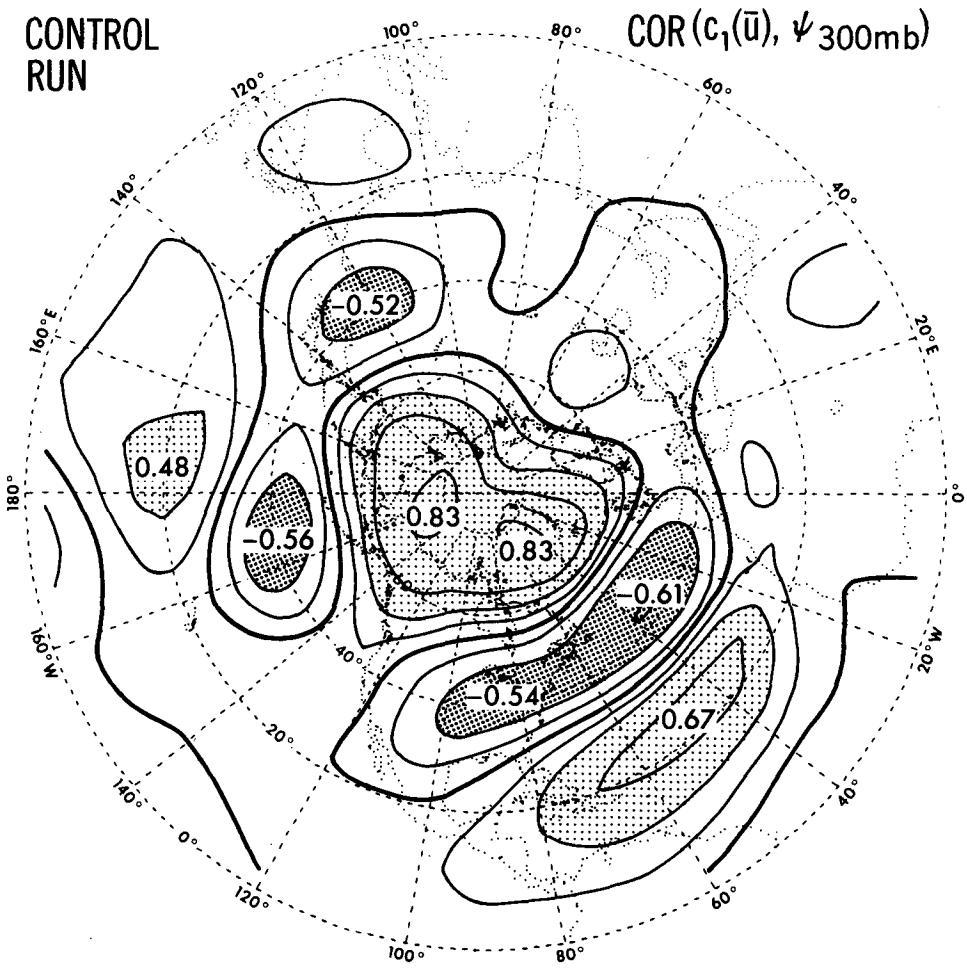

FIG. 10. Distribution of temporal correlation coefficients between the coefficients for $e_1(\bar{u})^{\text{CONTROL}}$ (Fig. 9) and 300-mb total streamfunction, as computed using monthly means for 15 northern winters in the control run. Contour interval 0.2.

These patterns (not shown) are largely similar to the corresponding charts for the SST run (shown in Fig. 8), and to the composite maps constructed by Lau (1981) on the basis of the leading combined three-variable eigenvector representing coherent changes in 500-mb, 850-mb temperature and 1000-mb height. Specifically, positive $c_1(\bar{u})^{\text{CONTROL}}$ are accompanied by

- a north–south seesaw in sea-level pressure between the midlatitude oceans and the Arctic (see Fig. 8a, this paper; and Lau, 1981, Fig. 15c);
- east–west temperature seesaws between northern Europe and Greenland, and between southeast and northwest quadrants of the North American continent (see Fig. 8b, this paper; and Lau, 1981, Fig. 16);
- enhanced precipitation over the Pacific and Atlantic within the 30°–40°N latitude belt, and dryness in the regions farther south and farther north (see Fig. 8c, this paper; and Lau, 1981, Fig. 18b).

Furthermore, it is seen that $e_1(\bar{u})^{\text{CONTROL}}$ is not linked to any significant anomaly pattern in the tropics.

8. Discussion

Altogether two types of characteristic circulation patterns have been identified in the model atmosphere. The first type (Fig. 1a) bears a striking resemblance to the PNA pattern observed in the atmosphere. This mode is discernible in the SST runs, but not in the control run, indicating the important role of SST variability in forcing this pattern. This notion is reinforced by the demonstrable temporal correlation of this mode with the SST anomalies imposed in the tropical Pacific, and with various well-known global atmospheric changes accompanying ENSO. The second type of anomaly pattern (Figs. 1b and 11) is detectable in both the SST and control runs, and is closely related to fluctuations in the zonally averaged zonal flow. The family of simulated anomalies associated with the second type have also been observed in the real atmosphere. Among such features are the seesaws in temperature and surface pressure in the Northern Hemisphere extratropics, as well as migration of the baroclinic zones and jet streams associated with variations of the zonal index. Com-

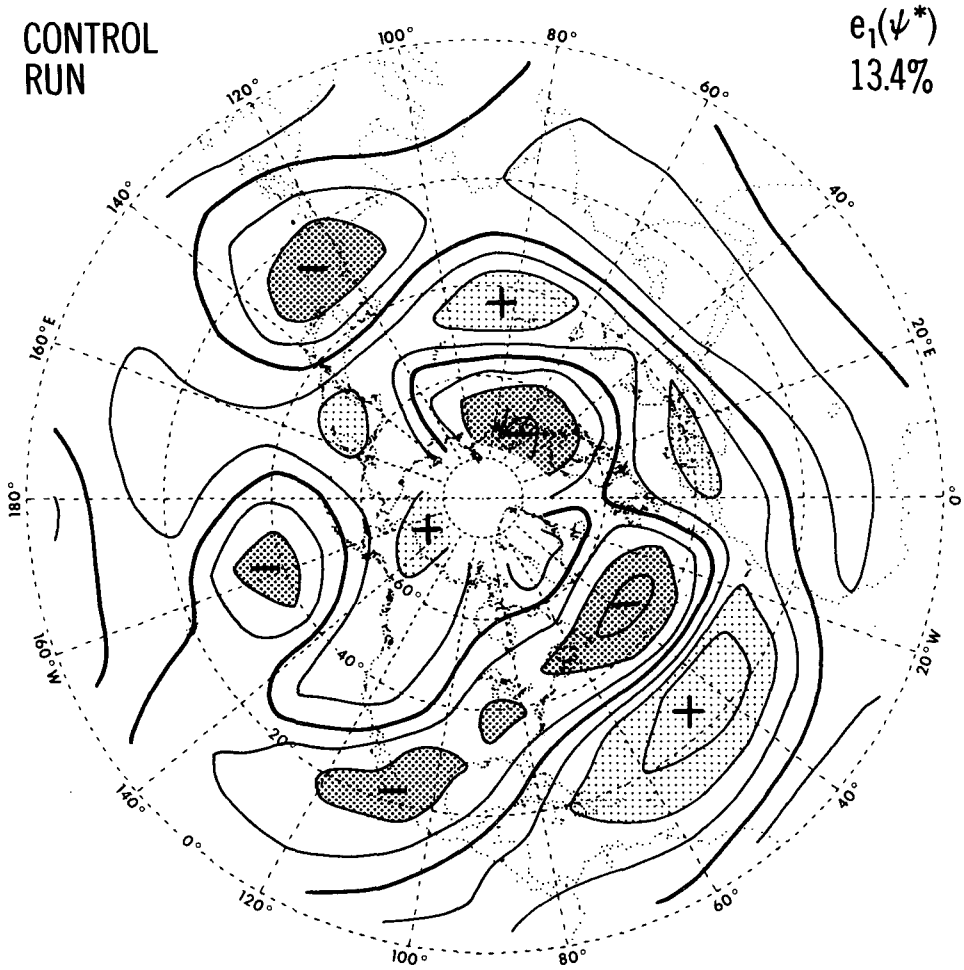

FIG. 11. Distribution of the first eigenvector of the 300-mb eddy streamfunction, $e_1(\psi^*)^{\text{CONTROL}}$, as computed using monthly means for 15 northern winters in the control run. Arbitrary units.

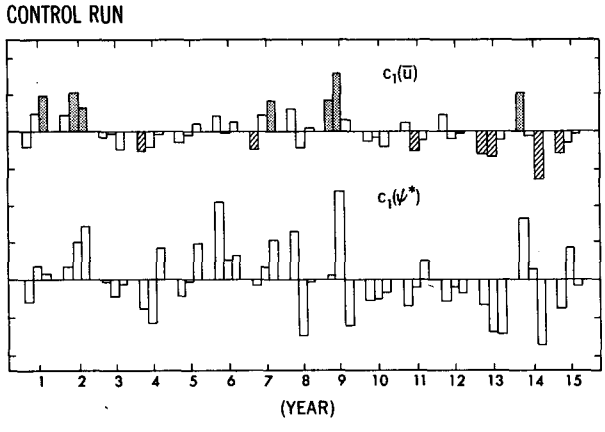

FIG. 12. Temporal variations during the 15 winters in the control run of the coefficients for $e_1(\bar{u})^{\text{CONTROL}}$ (upper-half); and of the coefficients for $e_1(\psi^*)^{\text{CONTROL}}$ (lower-half). Arbitrary units. Those 7 months with the most positive (negative) coefficients for $e_1(\bar{u})^{\text{CONTROL}}$ are identified by stippled (striped) columns in the upper-half, and used to construct the composite charts in Fig. 13.

parison between the findings reported here and those in Lau (1981) indicates that the principal mode of variability described in that earlier study belongs to the second type. The presence of this mode in a model environment with nonchanging boundary forcing suggests that internal atmospheric processes may play a substantial role.

Judging from the cumulative evidence presented in Lau (1981, 1985), and the present paper, one sees that a more balanced view of the multiple causes of variability in the model atmosphere begins to emerge. The results in this series of model experiments imply that both internal atmospheric processes and external forcing are capable of imparting a considerable level of variability to the atmospheric circulation. Outside of the tropics, the amplitudes of the patterns associated with SST changes (see Fig. 3) and with zonal/eddy interaction (Figs. 7a and 13a) are quite comparable. The distinction between extratropical responses to anomalous boundary forcing and to internal dynamics

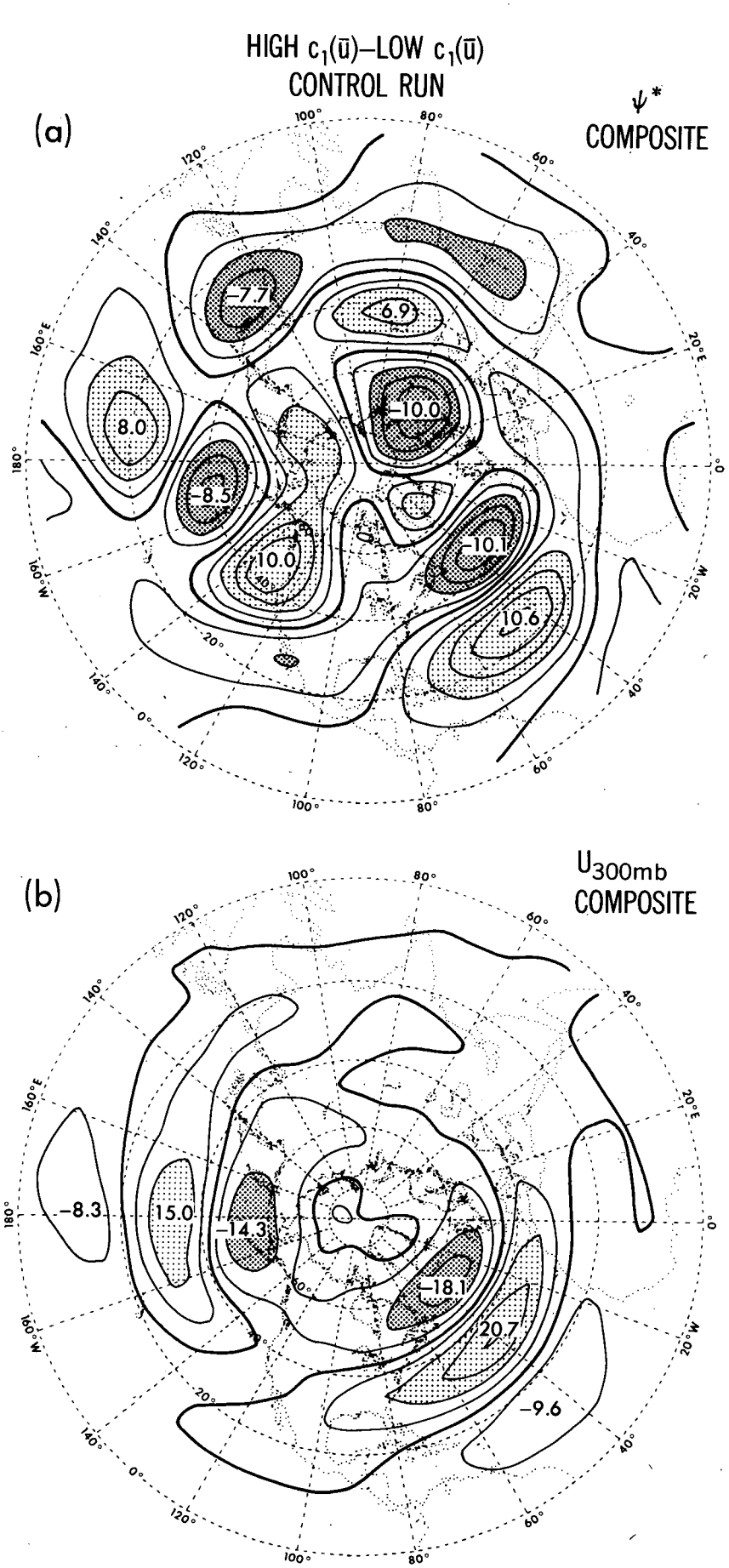
HIGH $c_1(\bar{u})$–LOW $c_1(\bar{u})$
CONTROL RUN
(a)
ψ^*
COMPOSITE
-7.7
6.9
8.0
-10.0
-8.5
10.0
-10.1
10.6
(b)
U_{300mb}
COMPOSITE
-8.3
15.0
-14.3
-18.1
20.7
-9.6

FIG. 13. As in Fig. 7, except for composites constructed on the basis of coefficients of $e_1(\bar{u})^{\text{CONTROL}}$ (stippled and striped columns in the upper-half of Fig. 12).

mainly lies in the detailed *spatial structure* of the characteristic circulation patterns, rather than in the *amplitude* of the perturbations. On the other hand, variability in the tropics is seen to be strongly influenced by the presence of El Niño episodes, the effect being manifest both in the fluctuation amplitude and in the character of the spatial pattern.

In conclusion, the additional diagnoses performed here have yielded some fresh insights into the origin of anomalous model behavior reported in the previous investigations on the control and SST runs (Manabe and Hahn, 1981; Lau, 1981, 1985). The results presented have also identified several research issues worthy of further pursuit. Among such issues are the mechanisms linking midlatitude circulation anomalies to tropical SST changes, the dynamical processes associated with the zonal/eddy relationship, and the causes of variability in the zonally averaged circulation itself. Advances in these problem areas will, no doubt, contribute to our ongoing quest for a comprehensive understanding of atmospheric variability.

Acknowledgments. We should like to thank Dr. I. M. Held for helpful discussions and encouragement in the course of this investigation. We also wish to thank Drs. A. H. Oort and I. M. Held for reading the manuscript, and Drs. S. Manabe and T. Matsuno for several stimulating discussions concerning the present work; the official reviewers for their constructive comments, Ms. J. Kennedy for typing the manuscript, and the GFDL Scientific Illustration Group for drafting the figures. The first author (ISK) was supported by NOAA/Princeton University under Grant NA84-EAD00057.

REFERENCES

Arkin, P. A., 1982: The relationship between interannual variability in the 200 mb tropical wind field and the Southern Oscillation. *Mon. Wea. Rev.*, **110**, 1393–1404.

Bjerknes, J., 1966: A possible response of the atmospheric Hadley circulation to equatorial anomalies of ocean temperature. *Tellus*, **18**, 820–829.

——, 1969: Atmospheric teleconnections from the equatorial Pacific. *Mon. Wea. Rev.*, **97**, 163–172.

Branstator, G., 1984: The relationship between zonal mean flow and quasi-stationary waves in the midtroposphere. *J. Atmos. Sci.*, **41**, 2163–2178.

Chen, W. Y., 1982: Fluctuations in Northern Hemisphere 700 mb height field associated with the Southern Oscillation. *Mon. Wea. Rev.*, **110**, 808–823.

Geisler, J. E., M. L. Blackmon, G. T. Bates and S. Muñoz, 1985: Sensitivity of January climate response to the magnitude and position of equatorial Pacific sea surface temperature anomalies. *J. Atmos. Sci.*, **42**, 1037–1049.

Gordon, C. T., and W. F. Stern, 1982: A description of the GFDL global spectral model. *Mon. Wea. Rev.*, **110**, 625–644.

Horel, J. D., and J. M. Wallace, 1981: Planetary scale atmospheric phenomena associated with the Southern Oscillation. *Mon. Wea. Rev.*, **109**, 813–829.

Kutzbach, J. E., 1967: Empirical eigenvectors of sea-level pressure, surface temperature and precipitation complexes over North America. *J. Appl. Meteor.*, **6**, 791–802.

——, 1970: Large-scale features of monthly mean Northern Hemisphere anomaly maps of sea-level pressure. *Mon. Wea. Rev.*, **98**, 708–716.

Lau, N.-C., 1981: A diagnostic study of recurrent meteorological anomalies appearing in a 15-year simulation with a GFDL general circulation model. *Mon. Wea. Rev.*, **11**, 2287–2311.

——, 1985: Modeling the seasonal dependence of the atmospheric response to observed El Niños in 1962–76. *Mon. Wea. Rev.*, **113**, 1970–1996.

——, and A. H. Oort, 1985: Response of a GFDL general circulation model to SST fluctuations observed in the tropical Pacific Ocean during the period 1962 to 1976. *Coupled Ocean-Atmosphere Models*, Chap. 21, J. Nihoul, Ed., Elsevier Oceanography Series, Amsterdam, 767 pp.

Manabe, S., and D. G. Hahn, 1981: Simulation of atmospheric variability. *Mon. Wea. Rev.*, **109**, 2260–2286.

Namias, J., 1950: The index cycle and its role in the general circulation. *J. Meteor.*, **7**, 130–139.

——, 1969: Seasonal interactions between the North Pacific Ocean and the atmosphere during the 1960s. *Mon. Wea. Rev.*, **97**, 173–192.

Palmer, T. N., and D. A. Mansfield, 1984: Response of two atmospheric general circulation models to sea-surface temperature anomalies in the tropical East and West Pacific. *Nature*, **310**, 483–485.

Rasmusson, E. M., and T. H. Carpenter, 1982: Variations in tropical sea surface temperature and surface wind fields associated with the Southern Oscillation/El Niño. *Mon. Wea. Rev.*, **110**, 354–384.

Rogers, J. C., and H. van Loon, 1979: The seesaw in winter temperatures between Greenland and northern Europe. Part II: some oceanic and atmospheric effects in middle and higher latitudes. *Mon. Wea. Rev.*, **107**, 509–519.

Rossby, C.-G., and H. C. Willett, 1948: The circulation of the upper troposphere and lower stratosphere. *Science*, **108**, 643–652.

Rowntree, P. R., 1972: The influence of tropical east Pacific Ocean temperatures on the atmosphere. *Quart. J. Roy. Meteor. Soc.*, **98**, 290–321.

van Loon, H., and J. C. Rogers, 1978: The seesaw in winter temperatures between Greenland and Northern Europe. Part I: General description. *Mon. Wea. Rev.*, **106**, 296–310.

——, and ——, 1981: The Southern Oscillation. Part II: Associations with changes in the middle troposphere in the northern winter. *Mon. Wea. Rev.*, **109**, 1163–1168.

Walker, G. T., and E. W. Bliss, 1932: World Weather V. *Mem. Roy. Meteor. Soc.*, **4**, 53–84.

Wallace, J. M., and M. L. Blackmon, 1983: Observations of low-frequency atmospheric variability. *Large Scale Dynamical Processes in the Atmosphere*, B. J. Hoskins and R. P. Pearce, Eds., Academic Press, 55–94.

——, and D. S. Gutzler, 1981: Teleconnections in the geopotential height field during the Northern Hemisphere winter. *Mon. Wea. Rev.*, **109**, 784–812.

Walsh, J. E., and C. M. Johnson, 1979: Interannual atmospheric variability and associated fluctuations in Arctic Sea ice extent. *J. Geophys. Res.*, **84**, 6915–6928.

——, D. R. Tucek and M. R. Peterson, 1982: Seasonal snow cover and short-term climatic fluctuations over the United States. *Mon. Wea. Rev.*, **110**, 1474–1485.

Webster, P. J., 1972: Response of the tropical atmosphere to local, steady forcing. *Mon. Wea. Rev.*, **100**, 518–540.

Yeh, T.-C., R. T. Wetherald and S. Manabe, 1984: The effect of soil moisture on the short-term climate and hydrology change—a numerical experiment. *Mon. Wea. Rev.*, **112**, 474–490.